POLITECNICO
MILANO 1863

SCUOLA DI INGEGNERIA INDUSTRIALE
E DELL'INFORMAZIONE

Executive Summary of the Thesis

Label-Free and High-Speed Biomedical Imaging through Colocalized SHG and Broadband CARS Microscopy

Laurea Magistrale in Physics Engineering

Author: Claudio Cavecchi

Advisor: Prof.Dario Polli

Co-advisor: Dr.Federico Vernuccio

Academic year: 2022-2023

1. Introduction

Vibrational microscopy is a powerful imaging technique capable of distinguishing different chemical species in heterogeneous biological samples by detecting their vibrational spectrum. The vibrational spectrum reflects the molecular structure of the sample and provides a chemically specific signature that can be exploited for its identification. Vibrational microscopy overcomes the limitations of fluorescence microscopy since it investigates the chemical composition and structure of the sample in a label-free manner without the need for exogenous or endogenous markers.

The gold standard technique for vibrational microscopy is Spontaneous Raman (SR). SR utilizes an incoming quasi-monochromatic laser light at frequency ω_p (pump frequency) in the visible or near-infrared to excite the molecule to a virtual state. The molecule relaxes to the ground state, emitting a photon with lower energy at frequency ω_s (Stokes frequency). The Stokes frequency $\omega_s = \omega_p - \Omega$, with Ω being the vibrational resonance of the sample, is red-shifted in frequency and encodes the vibrational information. Despite providing high chemical specificity, thanks to the detection of the full spectrum, SR suffers from a low scattering cross-section, requiring long integration times for single-spectrum acquisition and preventing fast imaging speed.

Coherent Anti-Stokes Raman Scattering (CARS) provides higher imaging speed with respect to SR by exploiting the third-order non-linear optical response of the sample. CARS employs two synchronized trains of laser pulses at frequencies ω_s (Stokes) and ω_p (pump) to resonantly excite the Raman transition at frequency $\Omega = \omega_p - \omega_s$. When the frequency difference matches a resonance frequency Ω_R of the investigated sample, all the molecules in the focal spot are resonantly excited. Then, the vibrational mode is read by means of another interaction with the pump. The CARS signal will be emitted at the anti-Stokes frequency $\omega_{as} = 2\omega_p - \omega_s$ with an intensity from 6 to 7 orders of magnitude stronger than the SR one [1]. This configuration, called single-frequency CARS, enables video-rate imaging. However, it has limited information content since it can only probe a single vibrational transition, making it difficult to distinguish between different components in complex heterogeneous systems like cells and tissues with spectrally overlapped

chemical species. Broadband CARS (BCARS) addresses this limitation by combining the high acquisition speed of single-frequency CARS with the chemical specificity of SR. In the multiplex configuration, BCARS combines narrowband pump pulses with broadband Stokes pulses to generate a broadband anti-Stokes component, enabling the recording of broad vibrational spectra in one shot [2].
Second-Harmonic Generation (SHG) microscopy represents another pivotal microscopy modality. SHG involves the up-conversion of two lower energy photons to exactly twice the incident frequency. This process provides high sensitivity and specificity and optical sectioning capability for imaging bulk tissues in 3D. Since SHG is a second-order nonlinear optical mechanism, its sensitivity is exclusively directed towards non-centrosymmetric structures on the scale of the SHG wavelength. As a result, SHG exhibits pronounced sensitivity, particularly towards collagen structures, a group of proteins present in most connective tissues [3]. At the molecular level, collagen comprises three α chains, known as tropocollagen, which are held together by hydrogen bonds. In certain types of collagen, particularly types I and II, these triple helices spontaneously self-organize into well-structured collagen fibrils, leading to robust SHG signals. Conversely, non-fibrillar collagen, which forms sheets in basal laminae, cannot be imaged with SHG microscopy.
This thesis focuses on utilizing and improving a BCARS set-up to convert it into a versatile multimodal microscope capable of simultaneously detecting BCARS and SHG signals in order to deliver more detailed chemical maps. The thesis also introduces post-processing methods for data analysis, with the aim of obtaining spectra comparable to those achieved with SR, along with the capability to distinguish the various chemical constituents within the biological sample through false-color images.

2. Theory

When the peak intensity of the pulse that is propagating in the medium has a value between $10^9 \frac{W}{cm^2}$ and $10^{12} \frac{W}{cm^2}$, the response of the medium is non-linear. In this situation, the polarization can be written as the sum of the linear $P^{(l)}$ and non-linear polarization $P^{(nl)}$: $P = P^{(l)} + P^{(nl)}$. The non-linear polarization can be further developed as the sum of many components with different orders of non-linearity:

$$P^{(nl)} = P^{(2)} + P^{(3)} + ... \tag{1}$$

SHG arises from second-order non-linear polarization:

$$P^{(2)} = \epsilon_0 \chi^{(2)} E^2 \tag{2}$$

where $\chi^{(2)}$ is the second-order susceptibility. When two waves of frequency ω interact with a nonlinear medium, they generate a second-harmonic (SHG) wave at a frequency of 2ω. The intensity of this SHG wave can be formulated as follows:

$$I_{SHG}(L) \propto I_{in}^2 L^2 sinc^2\Big(\frac{\Delta k L}{2}\Big) \tag{3}$$

where I_{in} is the intensity of the incident laser beam, L is the length over which SHG occurs in the medium, and $\Delta k = 2k_\omega - k_{2\omega}$ represents the phase mismatch between the excitation and the emitted light wavenumber.
On the other hand, CARS arises from third-order non-linear polarization:

$$P^{(3)} = \epsilon_0 \chi^{(3)} E^3 \tag{4}$$

where $\chi^{(3)}$ is the third-order susceptibility. Following the interactions of the pump field and of the Stokes fields with the medium in a four-wave mixing (FWM) process, the anti-Stokes component is generated, and its intensity is as follows:

$$I_{CARS} \propto |\chi^{(3)}|^2 I_p^2 I_s L^2 \tag{5}$$

where I_p represents the pump intensity, I_s denotes the Stokes intensity, and L corresponds to the length of the medium. This formulation remains valid when subject to the constraint of tight focusing, where $\Delta \boldsymbol{k} = 2\boldsymbol{k}_p - \boldsymbol{k}_s - \boldsymbol{k}_{as} \approx 0$, a condition readily justifiable in microscopy applications. The CARS intensity is proportional to $|\chi^{(3)}|^2$, where $\chi^{(3)}$ can be written as the sum of a resonant and a non-resonant parts: $\chi^{(3)} = \chi^{(3)}_{NR} + \chi^{(3)}_R$. The resonant part $\chi^{(3)}_R$ is the superposition of several complex Lorentzian responses related to the different vibrational transitions of the molecules so that it can be written as:

$$\chi^{(3)}_R(\omega) = \sum_i \frac{N_i \sigma_i}{\omega - \Omega_i - i\Gamma_i} \tag{6}$$

where N_i is the density of vibrational oscillators, σ_i is the cross-section, Ω_i the resonance frequency, and Γ_i the homogenous linewidth of the i-th vibrational transition. The non-resonant susceptibility $\chi^{(3)}_{NR}$ is pure real and constant in frequency considering working wavelengths far from electronic resonances. The CARS intensity dependence on the square modulus of $\chi^{(3)}$ can be developed as:

$$I_{CARS} \propto |\chi^{(3)}_R|^2 + |\chi^{(3)}_{NR}|^2 + 2\chi^{(3)}_{NR}\mathbb{R}e\left\{\chi^{(3)}_R\right\} \tag{7}$$

Analyzing equation (7), it is possible to observe that the CARS intensity is the sum of three different contributions:

- The resonant term $|\chi^{(3)}_R|^2$ contains information regarding the vibrational modes.
- The non-resonant term corresponds to $|\chi^{(3)}_{NR}|^2$. This term is a frequency-independent contribution to the signal unless it is close to electronic resonances.
- The last term, $2\chi^{(3)}_{NR}\mathbb{R}e\left\{\chi^{(3)}_R\right\}$, arises from the interference between the resonant and non-resonant contributions, giving rise to a dispersive signal distorting the line shape.

The interference term between the resonant and non-resonant components causes the CARS spectrum to deviate from the SR spectrum. In fact, the second and third terms of the equation (7) generate the so-called non-resonant background (NRB). The NRB has a dual effect on the signal: it provides a heterodyne amplification of the signal, but it also alters the Lorentzian shape of the peaks by introducing a dispersive component that shifts the peak maxima to lower frequencies and creates a dip at higher frequencies of the Raman peak. The resonant term is the only part of the CARS signal that contains information about the vibrational modes and is useful for spectroscopic applications. Therefore, it is often desirable to extract the imaginary part of $\chi^{(3)}_R$, which has a Lorentzian shape, from the CARS signal. This is possible by exploiting the Kramers-Kroning (KK) relations [4].

In our system to record the whole vibrational spectrum, we employed the "two-color" and "three-color" CARS mechanisms. In the two-color model, the vibrational coherence is produced through one interaction with a narrowband pump pulse and another interaction with a broadband Stokes pulse and is subsequently detected via a further interaction with the narrowband pump, acting as a probe, which generates the anti-Stokes signal. This mechanism allows us to cover the region between 1400 and 3200 cm^{-1} of the spectrum. In contrast, the three-color mechanism generates the vibrational coherence directly via the Impulsive Stimulated Raman Scattering (ISRS) process, whereby different frequency components of a single broadband pulse excite virtual levels and stimulate the emission down to vibrational levels of the ground state, creating a vibrational coherence in all modes whose oscillation period is comparable to or longer than the duration of the excitation laser pulse. The vibrational coherence can then be read out by interacting with the narrowband pump pulse. This mechanism allows us to cover the region of the spectrum up to 1400 cm^{-1}.

3. Experimetal setup

My thesis focuses on advancing the application of an experimental BCARS setup that has been previously used in other publications [5, 6]. Notably, I have made a distinctive contribution by enhancing its performance through the creation of a multimodal microscope capable of concurrently acquiring BCARS and SHG signals. The BCARS experimental setup comprises three primary components: the light sources, the microscope, and the detection. A schematic representation of the setup is shown in Figure 1.

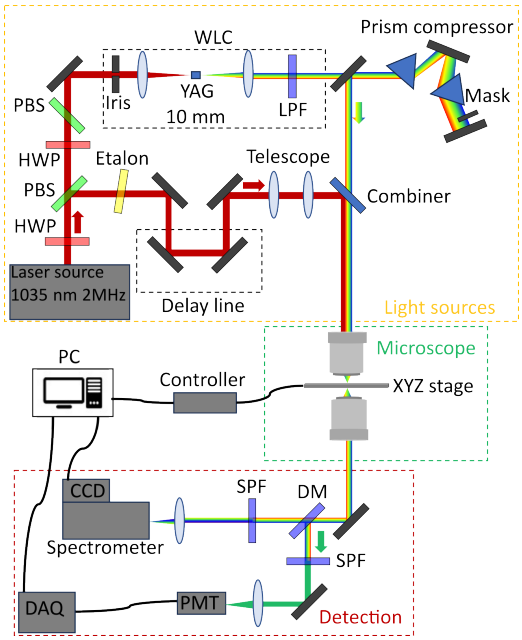

Figure 1: Scheme of the experimental setup.

The system starts with a 2-MHz repetition rate fiber-based Ytterbium laser system (Monaco 1035, Coherent) that delivers pulses of approximately 270-femtoseconds duration with a spectral bandwidth of 10 nm, centered at a wavelength of $\lambda_0 = 1035$ nm. The laser output is divided into two branches using a polarizing beam splitter (PBS) and a half-wave plate (HWP). The first replica passes through an etalon, which shrinks the bandwidth, generating narrowband pump pulses. The second beam replica is employed to generate a White-Light Continuum (WLC) in a YAG crystal. This WLC serves as the broadband Stokes pulse. The chirp of the broadband beam is compensated by a prism-pair compressor. The spatiotemporal overlap between the two pulse trains is achieved by employing a manual delay line mounted on the pump beam path. Subsequently, the light passes through a home-built microscope, which focuses the two beams onto the sample plane and collimates the transmitted BCARS beam. The BCARS signal is focused on a spectrometer that separates the different frequencies. Then, the various frequencies reach a high-speed back-illuminated deep-depletion CCD camera. The light is focused on the sample in a raster-scanning modality using a stepper-motor controller, allowing fast imaging speed. In order to transform the setup into a multimodal platform, I implemented a series of modifications. To acquire the SHG signal primarily from the pump but also from the Stokes after passing through the sample, I mounted a dichroic mirror (DM) after the microscope. The dichroic mirror allows the transmission of the BCARS signal toward the spectrometer while reflecting the SHG signals. To prevent any residual pump and Stokes signals from being detected, I used a short-pass filter (SPF) in order to selectively transmit wavelengths below 800 nm. Then, I installed a Photosensor Module equipped with a Photomultiplier Tube Module (PMT, H10721-110, Hamamatsu) to effectively capture the transmitted light. Then, I connected the PMT module, after passing through a trans-impedance used to integrate the signal, to a Data Acquisition (DAQ) system (NI USB-6341), enabling the acquisition of the SHG signals from the sample under investigation. Finally, I have developed a custom MATLAB script to enable the simultaneous acquisition of both BCARS and SHG signals.

4. Acquisition and processing of the CARS data

After the acquisition, the BCARS data underwent post-processing. Initially, the raw BCARS data were subjected to a preliminary denoising procedure, which I personally implemented, utilizing Singular Value Decomposition (SVD) and Fourier-transform techniques. Subsequently, the time-domain KK algorithm was employed to remove the NRB from the CARS spectra, extracting pure vibrational information. Finally, spectral unmixing algorithms were used to locate different chemical species in heterogeneous samples, such as Principal Component Analysis (PCA) in spectroscopic applications or methods such as N-FINDR and k-means cluster analysis in the case of CARS imaging.

5. Experimental results

To assess the performance of the BCARS system, I performed spectroscopy measurements on some solvents (toluene, isopropanol, methanol, ethanol, DMSO, and acetone) with a pixel dwell time of 1 ms and subcellular components (endoplasmic reticulum (ER), cytoplasm, nuclei, lysosomes, mitochondria, and mitochondria-associated membrane (MAM)) with a pixel dwell time of 50 ms. The initial raw BCARS data underwent the post-processing procedure. For solvents, the obtained spectra are compared to SR spectra, resulting in excellent agreement regarding the relative positions of the peaks and their amplitude ratios. On the other hand, for subcellular components, most of the spectral features observed in the SR spectra are also visible in the BCARS spectra, but some differences can be seen due to the different sample preparation and sample heterogeneity. Furthermore, the spectral profiles of subcellular components underwent a comparative analysis with measurements obtained from an alternative BCARS configuration situated at the IPHT; an example is shown in Figure 2. The high degree of similarity between the different measurements demonstrates the robustness and reliability of this technique in generating consistent and reproducible spectral data.

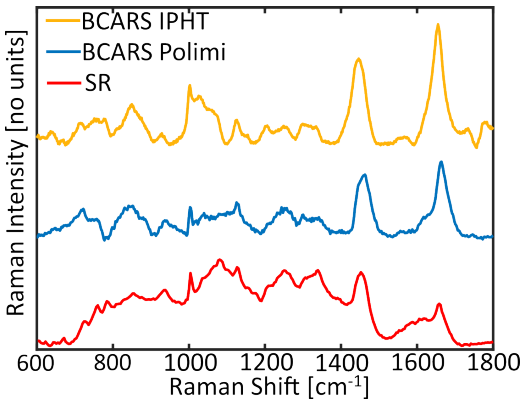

Figure 2: BCARS spectra of endoplasmic reticulum (ER) after NRB removal obtained at Polimi (blue line) and at IPHT (yellow line) and SR spectra (red line).

Another experiment that I performed was based on cellular segmentation to retrieve the average spectrum of cells belonging to two different tumor lines, HepG2 and HeK293. The average spectra of the HepG2 and HeK293 cells are presented in Figure 3.

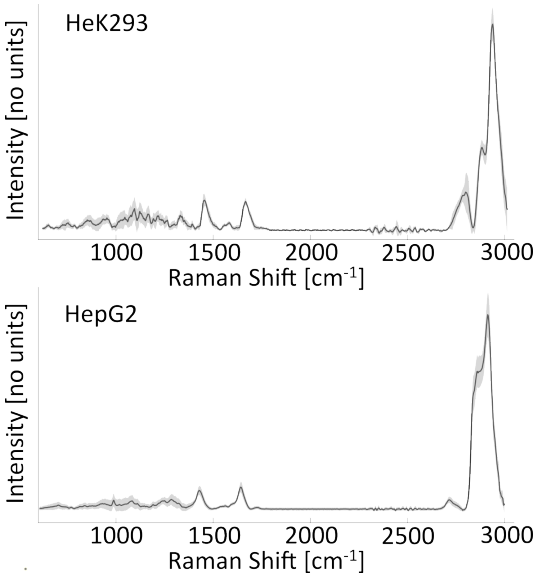

Figure 3: Average Raman spectra of the HepG2 and HeK293 cell lines, with the shaded gray region indicating the standard deviation at each Raman shift.

After the acquisition of the dataset of cell spectra, a statistical analysis based on PCA was performed. The projection of the data on the first two principal components, PC1 and PC2, is shown in Figure 4. The analysis shows that PC1, which accounts for most of the variability in the dataset, is able to distinguish different cells uniquely from their spectral characteristics. The fact that the other principal components accounted for only a small amount of variance suggests that the only factor capable of distinguishing between different cell types was the cell line. This outcome underscores the absence of any additional contributing factors to the variability within the dataset, such as artifacts, sample preparation, or experimental conditions. Finally, I proceeded to capture images

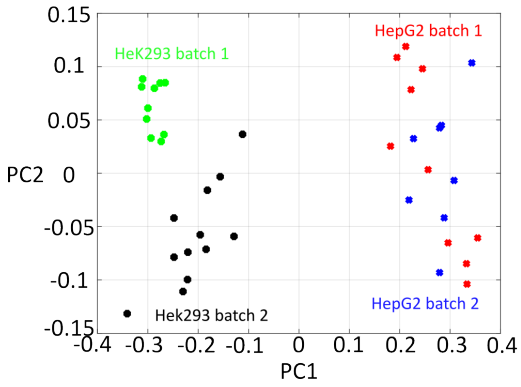

Figure 4: Projection of the data onto the first two principal components, PC1 and PC2.

of breast tissue samples containing microcalcifications by exploiting the multimodality that I incorporated into the experimental setup. My initial approach involved obtaining the BCARS signal as the first step. Subsequently, by shifting the central wavelength of the spectrometer to 500 nm, I acquired the SHG signal. However, this approach required an extended acquisition time for the acquisition of the two channels (8 ms/pixel for BCARS imaging + 15 ms/pixel for SHG imaging). To address this issue, I introduced the SHG channel, enabling the simultaneous acquisition of both BCARS and SHG signals without hampering the overall acquisition speed. After the acquisition, the BCARS image is subjected to a denoising process utilizing SVD, followed by the application of the time-domain KK algorithm to eliminate the NRB. After data processing, I used the N-FINDR algorithm to extract the main endmembers and the relative concentration maps (see Figure 5). From the analysis of the spectral features, I determined that the red endmember is associated with proteins, while the green one is associated with lipids. I also overlapped the SHG signal in blue, which highlights the collagen-rich regions, as shown in Figure

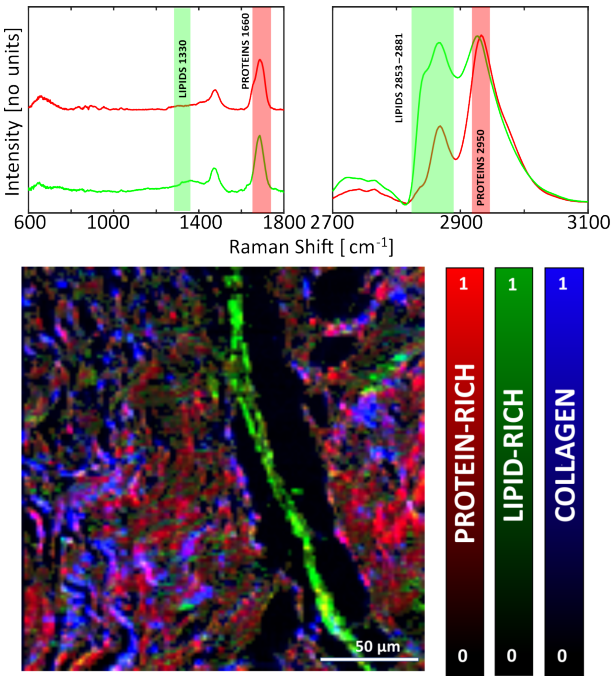

Figure 5: Spectra and concentration maps of the two endmembers are represented in different colors. Additionally, the concentration map of collagen is presented in blue.

Using the SHG map and the spectral information provided by BCARS, I extracted the collagen spectrum, depicted in Figure 6.

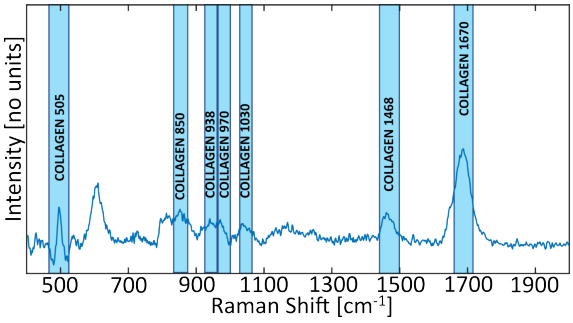

Figure 6: Retrieved spectra of collagen in the fingerprint region, with a focus on highlighting the characteristic peaks specific to collagen.

This information could not be retrieved using the N-FINDR algorithm due to the overlapping signal from collagen with non-collagen protein-rich regions. The spectrum obtained exhibits the characteristic collagen peaks (at 505 cm^{-1}, 850 cm^{-1}, 938 cm^{-1}, 970 cm^{-1}, 1030 cm^{-1}, 1468 cm^{-1}, and 1670 cm^{-1}), verifying the accuracy of our measurements.

6. Conclusion

In this study, I showcased the capabilities of our experimental setup. It not only excels in performing high-speed BCARS spectroscopy and imaging with exceptional sensitivity but also extends its functionality to encompass multimodal microscopy. This addition allows for the simultaneous acquisition of both BCARS and SHG signals, thereby providing detailed chemical and morphological information on the investigated samples. Furthermore, our multimodal microscope not only improves imaging performance but also serves as a potent tool for investigating intricate tissue structures with precision and efficiency. The ability to access additional chemical insights, such as collagen concentration within tissues, holds the promise of advancing our understanding of tissue microenvironments and disease pathology. Consequently, the multimodal microscope emerges as a valuable asset in the realms of biomedical research and diagnostics, which will contribute significantly to scientific advancements and clinical applications.

References

[1] D. Polli et al. Broadband Coherent Raman Scattering Microscopy. *Laser Photonics Rev.*, 12(9):1800020, 2018.

[2] C. H. Camp Jr. et al. High-speed CARS imaging of biological tissues. *Nature Photonics*, 8(8):627–634, 2014.

[3] L. Mostaço-Guidolin et al. Imaging collagen in scar tissue: Developments in SHG microscopy for biomedical applications. *Int J Mol Sci*, 18:1772, 2017.

[4] C. H. Camp et al. Quantitative, comparable CARS spectroscopy: correcting errors in phase retrieval. *J Raman Spectrosc*, 47(4):408–415, 2015.

[5] F. Vernuccio et al. Fingerprint multiplex CARS at high speed based on supercontinuum generation and deep learning spectral denoising. *Optics Express*, 30(17):30135, 2022.

[6] F. Vernuccio et al. Full-spectrum CARS microscopy with ultrashort white-light continuum pulses. *J. Phys. Chem. B*, 127:4733–4745, 2023.